2-15-2008

Modeling, Simulation, and Experiments of Coating Growth on Nanofibers

C. B. Clemons

P. Hamrick

J. Heminger

K. L. Kreider

G. W. Young

See next page for additional authors

Modeling, simulation, and experiments of coating growth on nanofibers

C. B. Clemons,[1] P. Hamrick,[1] J. Heminger,[1] K. L. Kreider,[1] G. W. Young,[1,a)] A. Buldum,[2] E. Evans,[3] and G. Zhang[3]
[1]*Department of Theoretical and Applied Mathematics, University of Akron, Akron, Ohio 44325-4002, USA*
[2]*Department of Physics, University of Akron, Akron, Ohio 44325-4001, USA*
[3]*Department of Chemical Engineering, University of Akron, Akron, Ohio 44325-3906, USA*

(Received 2 August 2007; accepted 4 December 2007; published online 26 February 2008)

This work is a comparison of modeling and simulation results with experiments for an integrated experimental/modeling investigation of a procedure to coat nanofibers and core-clad nanostructures with thin film materials using plasma enhanced physical vapor deposition. In the experimental effort, electrospun polymer nanofibers are coated with metallic materials under different operating conditions to observe changes in the coating morphology. The modeling effort focuses on linking simple models at the reactor level, nanofiber level and atomic level to form a comprehensive model. The comprehensive model leads to the definition of an evolution equation for the coating free surface around an isolated nanofiber. This evolution equation was previously derived and solved under conditions of a nearly circular coating, with a concentration field that was only radially dependent and that was independent of the location of the coating free surface. These assumptions permitted the development of analytical expressions for the concentration field. The present work does not impose the above-mentioned conditions and considers numerical simulations of the concentration field that couple with level set simulations of the evolution equation for the coating free surface. Further, the cases of coating an isolated fiber as well as a multiple fiber mat are considered. Simulation results are compared with experimental results as the reactor pressure and power, as well as the nanofiber mat porosity, are varied. © *2008 American Institute of Physics*. [DOI: 10.1063/1.2840137]

I. INTRODUCTION

This article is a continuation of Refs. 1–3. Those works presented a coordinated experimental and modeling program for the synthesis of core/clad and hollow nanowire structures. Physical vapor deposition techniques were used to apply coatings to electrospun polymer nanofibers. These fibers have been coated with films of copper, aluminum, titanium, zirconium, and aluminum nitride by using a plasma enhanced physical vapor deposition (PEPVD) sputtering process as shown in Fig. 1.[4] The present work benchmarks modeling and simulation results with experimental results as the reactor pressure and power, as well as the nanofiber mat porosity, are varied.

For reference, some details of the reactor and the synthesized nanowires are described. In the reactor, a power supply drives a 2 in. diameter electrode that forms the target (or source) material. A mat of nanofibers is placed on a holder that sits 8 cm above the target. When a negative electrical potential is applied to the electrode (target), a plasma of positively charged ions forms in the gas phase. The resulting electric field causes these ions to impact the target. These collisions, in turn, sputter neutral species of the target material into the gas phase. Once in the gas phase, the neutral species are transported throughout the reactor and are deposited on all available surfaces, including the nanofibers. Ions from the plasma also strike the coated nanofibers, but typically with much less energy because the substrate is not biased. These collisions tend to smooth out the coating through a re-sputtering process. The coating growth rate depends on the rate at which atoms are supplied to the nanofiber surface, the nanofiber temperature, and the ion flux to the nanofiber. The morphology of the coating depends on the mobility of the atoms on the surface and how much time the atoms have to move around before the next atoms hit the surface. The rate at which atoms are supplied to a nanofiber is proportional to the rate at which atoms are sputtered from the target and how far away the nanofiber is from the target. The sputtering rate depends on the ion flux, which is determined by the power applied to the target, the pressure of the system, and the working gas used.[4]

Transmission electron microscopy (TEM) is used to determine the effects of these variables on the film growth rate and morphology. The average thicknesses of the fibers before and after the coating process are compared to determine an average growth rate of the coating. TEM images are also used to evaluate the roughness of the coating.

Figures 2(a)–2(c) show nanofibers coated with aluminum. Following deposition, the polymer nanofiber may be removed by pyrolisis, leaving the outer coating. The approximate thickness of the coating was controlled by the sputtering process. Figures 2(a)–2(c) show that different coating morphologies, nodular versus wavy, are obtained. Modeling and simulation of these morphologies was the subject of Ref.3.

The above-described approach can be used to produce

a)Electronic mail: gwyoung@uakron.edu.

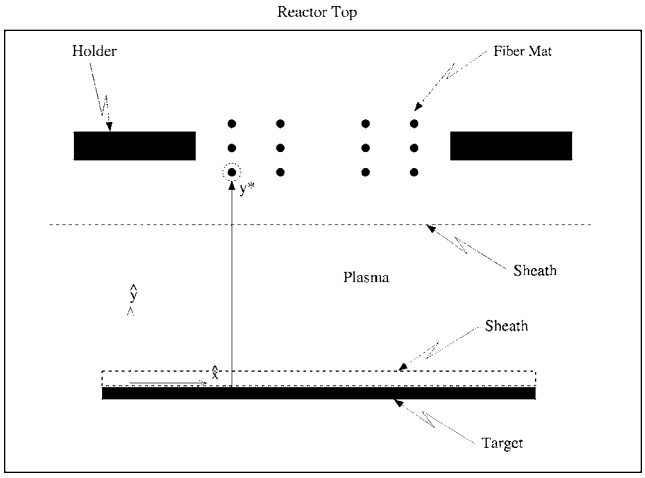

FIG. 1. Global schematic of the reactor for neutral species transport within the reactor.

cylindrical, multilayered, nanostructures with precisely controlled interfaces composed of many materials including metals, semiconductors, ceramics, and polymers with controlled diameters and a range of nanometer thickness walls.

II. SINGLE FIBER COATING MODEL

To aid the understanding of the deposition process, a comprehensive model for the coating of nanofibers within a traditional PEPVD system was described in Refs. 1–3. The objective of the model is to determine the influence of process conditions on the uniformity and morphology of the coating. The system is characterized by a bulk gas phase dominated by neutral species and sheath regions that separate the bulk gas phase from the substrate (nanofibers) and the target, as shown in Fig. 1. In the modeling effort, each nanofiber within the mat is treated as an isolated fiber. We modify the single fiber coating model to a multiple fiber setting in Sec. III.

The transport of neutral species is separated into two components: (1) A one-dimensional reactor-scale model and (2) a two-dimensional local nanofiber-scale model. The reactor-scale model, the focus of Ref. 1, includes the sheath region near the target and transport throughout the reactor, but ignores the presence of the holder region. Reference 2 focuses upon the transport of neutral species in the vicinity of a typical nanofiber. The two articles are linked as follows: the reactor-scale model provides the far-field (half the distance away from an adjacent fiber) input of the neutral species concentration, C^*, at location $\hat{y}=y^*$ of a particular nanofiber as shown in Fig. 1. Figure 3 provides a schematic of the region near a nanofiber. The cylindrical fiber is encapsulated by a nonuniform coating of neutral species. Outside the coating we suppose a sheath region exists and that the far field neutral species concentration is C^*. We note that the reactor-scale model[1] predicts that this concentration is constant throughout the reactor, except, of course, in the vicinity of the fiber.

At the local nanofiber scale, a polar coordinate geometry is considered in Ref. 2, whereas an axisymmetric geometry is discussed in Ref. 3. Level set and evolution equation approaches are used to simulate the coating shape. Four basic components of the coating mechanism are included in these approaches. These are attachment kinetics, curvature effects, etching due to ion bombardment, and surface diffusion on the coating front. These equations are solved numerically. The initial polymer nanofiber landscape is taken to be a superposition of Fourier modes, consistent with models of the electrospinning process.[5,6] Hence, our approach links models across the entire fabrication process. The next step is to

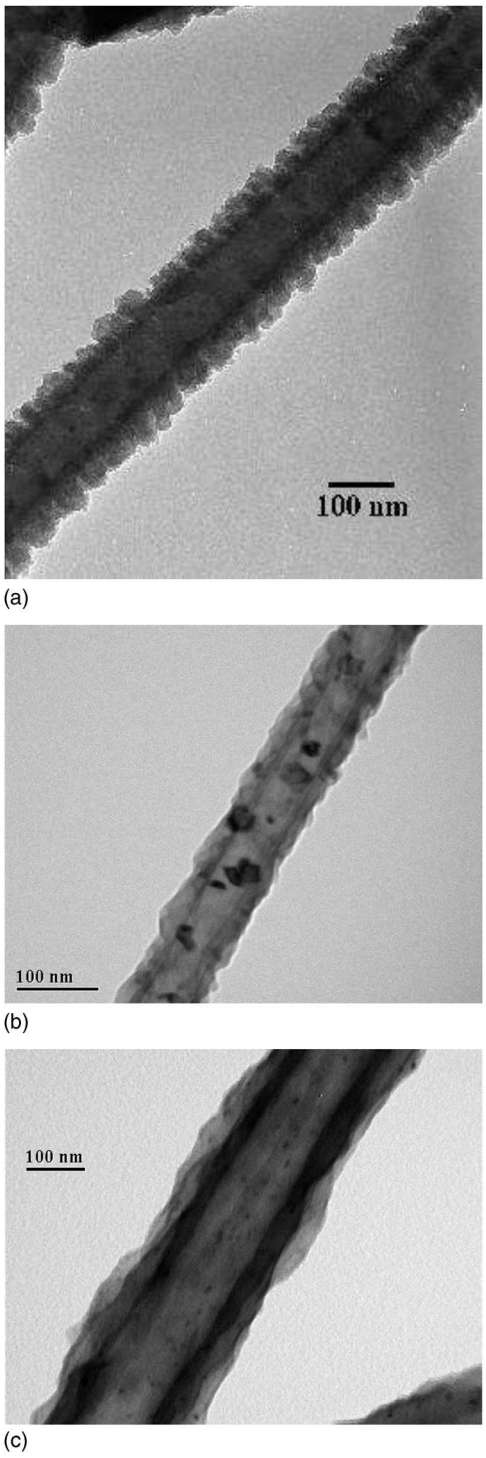

FIG. 2. TEM images of aluminum-coated nanofibers. (a) Nodular coating morphology, (b) wavy coating morphology on a small radius nanofiber, and (c) wavy coating morphology on a large radius nanofiber.

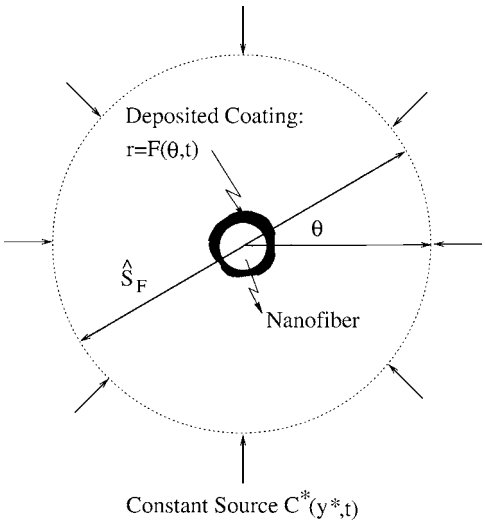

FIG. 3. Local model for neutral species transport near the nanofiber.

benchmark the model against experimental data as processing parameters are varied. This benchmarking is the subject of the present article.

A. Model formulation

In Ref. 1, the dimensional concentration C^* of the neutral species at the reactor scale was found to be the constant

$$C^* = \frac{k_{\text{ions}}}{k}, \tag{1}$$

where k is a reaction coefficient for sputtered material readsorbing to the target surface and k_{ions} is the desorption rate coefficient for sputtering due to ion bombardment of the target surface. These rate coefficients depend on the ion flux to the surface, and the ion kinetic energy. These two quantities were obtained by examining the sheath region around the target. These quantities are functions of the reactor pressure and power supplied to the target, which determine the ion number density, $\hat{n}_p$, in the plasma. The number density increases as the power and pressure increase as shown in Fig. 4, with the density being most sensitive to changes in the power.[7] The applied power and the pressure are both assumed controllable and therefore specified by the operator. Therefore, all constants that appear within this model are either material properties or can be experimentally controlled, at least in principle.

For $k_B = 1.38 \times 10^{-23}$ J/K the Boltzmann constant, q the ion charge, T the absolute temperature (in kelvin), and ε_0 the vacuum permittivity, the Debye length λ_D is given by

$$\lambda_D = \sqrt{\frac{\varepsilon_0 k_B T}{\hat{n}_p q^2}}. \tag{2}$$

The dimensionless constant

$$C_H = \frac{\alpha_H \lambda_D}{m} \tag{3}$$

represents the effect of collisions in slowing the ions. α_H measures the strength of the interaction between the ions and the background nonionized gas atoms or molecules, and m is

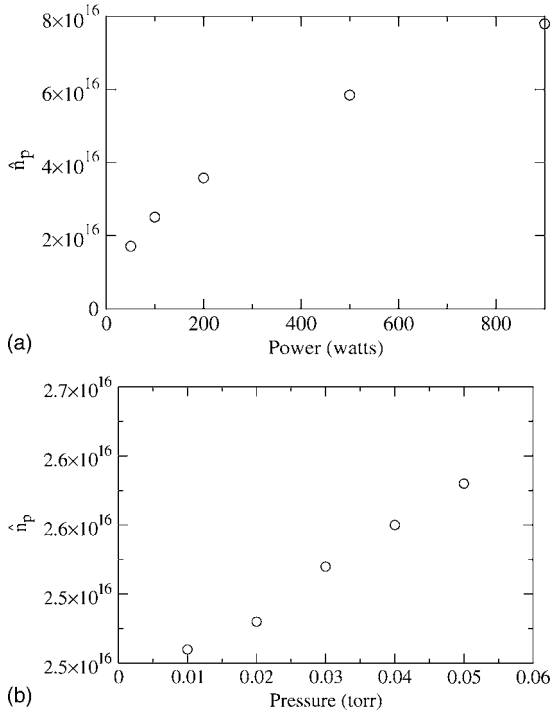

FIG. 4. Variation of the ion number density, $\hat{n}_p$, with power and pressure. (a) $\hat{n}_p$ vs power and (b) $\hat{n}_p$ vs pressure.

the mass associated with a single ion. As the pressure or power is increased, the ion number density $\hat{n}_p$ increases. As a result, the Debye length decreases and so the value of C_H also decreases. As the number of collisions decreases, the ion flux and kinetic energy increase. Although the value of k is less sensitive to changes in kinetic energy, the value of k_{ions} increases significantly with increasing kinetic energy. In turn the concentration of deposition material C^* increases. Numeric values for these results are listed in Figs. 6, 9, and 10 of Ref. 1. These values are used in the calculations in the following.

Hence, the concentration C^* is determined in the reactor as a function of the reactor operating conditions. This concentration field serves as the input for the local transport model as shown in Fig. 3. Given the sparsity of the nanofiber mesh, it is assumed that the concentration C^* away from a nanofiber is unaffected by any loss of depositing species due to deposition. However, the concentration near the nanofiber does change due to the deposition. Note also that the units of concentration are mole/volume, the units of k are length/time, and the units of k_{ions} are mole/(area × time).

For the local nanofiber scale transport model around a single nanofiber, consider a cylindrical geometry as shown in Fig. 3. This particular nanofiber is located at a distance $\hat{y} = y^*$ from the target as shown in Fig. 1. The goal is to determine the location, $\hat{r} = \hat{F}(\theta, \hat{t})$, of the front of the deposited coating. Assume the source of the deposition material is given by C^*, and is located at $\hat{r} = \hat{S}_F$, where $\hat{S}_F$ is half the average spacing between fibers in the mat. As C^* is a result of the sputtering process and depends on the reactor operating conditions, we have linked the *local and global* models through the condition at $\hat{r} = \hat{S}_F$.

Within the local region surrounding a fiber $[\hat{F}(\theta,\hat{t}) \leq \hat{r} \leq \hat{S}_F]$, assume that the concentration $\hat{c}$ of deposition material (neutral gas molecules) is large compared to the ion concentration, and that the mode of transport of the deposition material is primarily governed by diffusion,

$$\hat{c}_{\hat{t}} = \hat{D}\left[\hat{c}_{\hat{r}\hat{r}} + \frac{1}{\hat{r}}\hat{c}_{\hat{r}} + \frac{1}{\hat{r}^2}\hat{c}_{\theta\theta}\right], \tag{4}$$

where $\hat{D}$ is the diffusivity.

At the coating front $(\hat{r}=\hat{F}(\theta,\hat{t}))$, the diffusive flux of neutral species equals the net rate of deposition due to (i) deposition (or reaction) from the bulk phase and (ii) desorption due to ion bombardment of the coating surface. These two processes correspond to the respective terms on the right-hand side of the boundary condition

$$\hat{D}\,\nabla\,\hat{c}\cdot\hat{n} = k_F\hat{c}[1-\hat{\Gamma}\hat{\kappa}] - k_{F_{\text{ions}}}. \tag{5}$$

Here k_F is a reaction coefficient, $\hat{\Gamma}$ is the capillary length scale, $\hat{\kappa}$ is the curvature of the front, and $k_{F_{\text{ions}}}$ is the desorption rate coefficient due to ion bombardment of the coating surface. The latter two quantities also vary with the power and pressure similar to the previous discussion at the target, and are obtained from Figs. 7 and 10 of Ref. 2.

The normal velocity of the coating front, $\hat{v}_n$, is needed to simulate the film growth at this length scale, using the level set method. The normal front velocity is taken to be

$$\hat{v}_n = k_F\beta\hat{c}[1-\hat{\Gamma}\hat{\kappa}] - \beta k_{F_{\text{ions}}} - \psi_s D_s\hat{\Gamma}\frac{\partial^2\hat{\kappa}}{\partial\hat{s}^2}, \tag{6}$$

where β is the molar volume, $\hat{s}$ is the arclength along the coating front, and ψ_s is the thickness of the coating film that participates in the surface diffusion phenomenon. The units for β are determined by $\beta=(\text{mwt})(1/\text{density})=\text{vol/mole}$, where the density is that for the coating in the solid phase and mwt is the molecular weight of the coating material.

All of the terms in Eq. (6) are evaluated on the front, $\hat{r}=\hat{F}(\theta,\hat{t})$. The first two terms in this equation are the contributions to the normal velocity due to deposition and desorption, and the third term is diffusion along the coating surface. Here D_s is the diffusivity of the adatoms on the coating surface.

The coating surface is given by

$$\vec{\hat{r}}(\theta,\hat{t}) = \hat{F}(\theta,\hat{t})[\cos\theta\vec{i} + \sin\theta\vec{j}], \tag{7}$$

so that the curvature of the front is

$$\hat{\kappa}(\theta,\hat{t}) = \frac{\hat{F}^2(\theta,\hat{t}) + 2\hat{F}_\theta^2(\theta,\hat{t}) - \hat{F}(\theta,\hat{t})\hat{F}_{\theta\theta}(\theta,\hat{t})}{[\hat{F}_\theta^2(\theta,\hat{t}) + \hat{F}^2(\theta,\hat{t})]^{3/2}}. \tag{8}$$

The normal vector to the coating front is

$$\hat{n} = \frac{\langle \hat{F}_\theta\sin\theta + \hat{F}\cos\theta, -\hat{F}_\theta\cos\theta + \hat{F}\sin\theta\rangle}{\sqrt{\hat{F}_\theta^2 + \hat{F}^2}}. \tag{9}$$

The normal front velocity, $\hat{v}_n$, is also defined by

$$\hat{v}_n = \frac{d\vec{\hat{r}}}{d\hat{t}}\cdot\hat{n}. \tag{10}$$

Setting Eq. (6) equal to Eq. (10) allows one to develop an evolution equation for the shape of the coating front.

The governing equations and boundary conditions are nondimensionalized using the following scalings:

(1) $\hat{c}$: C^*,
(2) $\hat{r}$: $\hat{S}_F$,
(3) $\hat{t}$: $\hat{S}_F/(K_F\beta C^*)$, and
(4) $\hat{s}$ - arc length: $\hat{S}_F$.

where K_F is a constant representing the average value of k_F. Dimensionless variables are hatless. These scalings lead to the nondimensional groups: $D_{k_F}=(k_F\hat{S}_F)/\hat{D}$, $\Gamma=\hat{\Gamma}/\hat{S}_F$, and $Q_F=K_F\hat{S}_F\beta C^*/\hat{D}\ll 1$, where D_{k_F}, the Damköhler number, is the ratio of the rate of deposition on the fiber to the rate of neutral species transport by diffusion, and Q_F is the ratio of the rate of front motion to the rate of diffusion of the neutral species.

The nondimensional governing equation for concentration is

$$Q_F c_t = c_{rr} + \frac{1}{r}c_r + \frac{1}{r^2}c_{\theta\theta} \quad \text{for} \quad F(\theta,t) < r < 1. \tag{11}$$

Here, $F(\theta,t)=\hat{F}(\theta,\hat{t})/\hat{S}_F$ is the dimensionless coating thickness. We impose two spatial boundary conditions upon the concentration field. At the edge of the local region ($r=1$), the concentration is uniform as predicted by the reactor scale model:

$$c = 1. \tag{12}$$

At the edge of the coating $[r=F(\theta,t)]$, we apply the dimensionless version of Eq. (5):

$$\frac{c_r - (F_\theta/F^2)c_\theta}{\sqrt{1+(F_\theta/F)^2}} = D_{k_F}c[1-\Gamma\kappa] - \frac{k_{F_{\text{ions}}}\hat{S}_F}{C^*\hat{D}}, \tag{13}$$

where

$$\kappa = \frac{F^2 + 2F_\theta^2 - FF_{\theta\theta}}{[F^2+F_\theta^2]^{3/2}} \tag{14}$$

is the nondimensional curvature.

The coating front velocity, Eq. (6), in dimensionless form is

$$\frac{\langle F_t\cos\theta, F_t\sin\theta\rangle\cdot\langle(F\sin\theta)_\theta, (-F\cos\theta)_\theta\rangle}{\sqrt{F_\theta^2+F^2}} = \frac{k_F}{K_F}c[1 - \Gamma\kappa] - \frac{k_{F_{\text{ions}}}}{K_F C^*} - \frac{\psi_s D_s}{\beta C^* K_F\hat{S}_F^2}\Gamma\frac{\partial^2\kappa}{\partial s^2}. \tag{15}$$

Note that $\partial^2\kappa/\partial s^2 = (\kappa_\theta/\sqrt{F^2+F_\theta^2})_\theta/\sqrt{F^2+F_\theta^2}$ is the second derivative of the curvature with respect to arc length, and so Eq. (15) takes the form

$$\frac{FF_t}{\sqrt{F^2+F_\theta^2}} = \frac{k_F}{K_F} c[1-\Gamma\kappa] - \frac{k_{F_{\text{ions}}}}{K_F C^*} - \frac{\psi_s D_s \Gamma}{\beta C^* K_F \hat{S}_F^2} \frac{(\kappa_\theta/\sqrt{F^2+F_\theta^2})_\theta}{\sqrt{F^2+F_\theta^2}}. \quad (16)$$

A similar axisymmetric version of this evolution equation has been derived and solved in Ref. 3.

Reference 2 solves Eqs. (11)–(16) by assuming that c is independent of θ, and by evaluating Eq. (13) at r_F, the average initial radius of the uncoated nanofiber. Under these approximations, the concentration field is not affected by perturbations in the coating surface. These approximations are not made in the present numerical simulations.

B. Numerical simulations

The full concentration problem (11) is solved by second order finite differences[8] for the standard parameter set:

$$k_F = 4 \times 10^{12} \text{ nm/s},$$

$$C^* = 1.5 \times 10^{-36} \text{ mol/nm}^3,$$

$$\hat{\Gamma} = 0.0505 \text{ nm},$$

$$\psi_s D_s = 6.5 \times 10^{-3} \text{ nm}^3/\text{s},$$

$$\hat{D} = 4 \times 10^{13} \text{ nm}^2/\text{s},$$

$$\hat{S}_F = 300 \text{ nm},$$

$$k_{F_{\text{ions}}} = 5.58 \times 10^{-26} \text{ mol/nm}^2 \text{ s}. \quad (17)$$

In the full concentration model, the concentration should ideally be updated at every time step. The concentration at the front is used in the deposition term in the normal velocity expression (15), and hence is needed in the level set algorithm to determine $F(\theta,t)$. However, the concentration computation is CPU intensive, so it is advantageous to update the concentration only at regular intervals instead of every time step. We find that with time steps of $\Delta t = 10^{-5}$ s, the concentration can be updated every 100 time steps with no change in the growth and roughness results.

An example of the differences induced by the approaches in Ref. 2 is shown in the concentration fields at the fiber surface in Fig. 5. Although the general trends are similar, the simplified concentration field leads to an overall higher concentration near the front, and hence higher deposition and faster coating growth. It also leads to a more angular variation in the concentration, which yields a rougher coating surface. Thus, in all of the parameter studies conducted, the two concentration models provide similar trends in coating growth and roughness, but there is a significant quantitative difference in the results. Further results of the numerical simulations are discussed in Sec. IV.

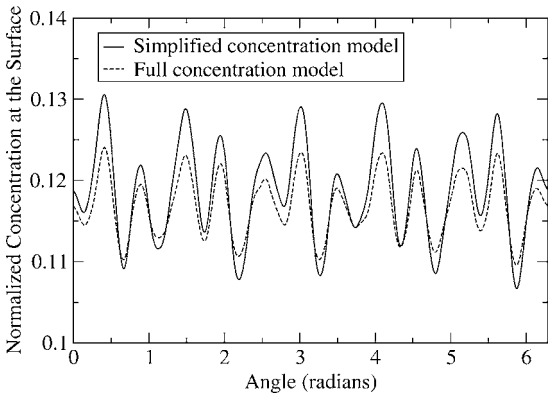

FIG. 5. A comparison of the concentration fields on the initial fiber surface for the simplified concentration model (Ref. 2) and the full numerical simulation.

III. MULTIPLE FIBER COATING MODEL AND RESULTS

We modify the single fiber coating model to a multiple fiber setting. This will help to determine the range of validity of the single fiber model, and give insight into the deposition differences between a high and low porosity fiber mat. For example, in Fig. 6 at locations where the fibers are close or cross, and the coating has become thick enough for noticeable changes in the coating thickness, one can see a pinching off of the coating. This pinching off indicates that the adjacent fibers are influencing the concentration field around the fibers.

A. Governing equations and solution procedure

For the multiple fiber configuration we consider a two-dimensional coating problem on a rectangular region R with seven fibers F oriented perpendicular to the region as shown in Fig. 7. The lower boundary S is the source of coating material. We assume the coating material diffuses throughout the region and coats the boundary ∂F of the fibers. In this formulation the location of F is fixed for mathematical simplicity to avoid the free boundary problem for determining the coating surfaces of the multiple fibers. At the remaining boundary $\partial R - S - \partial F$ of the region R we assume no flux conditions. Let c represent the concentration of the coating material at (x,y) and time t Let $\mathbf{n}$ represent the unit normal

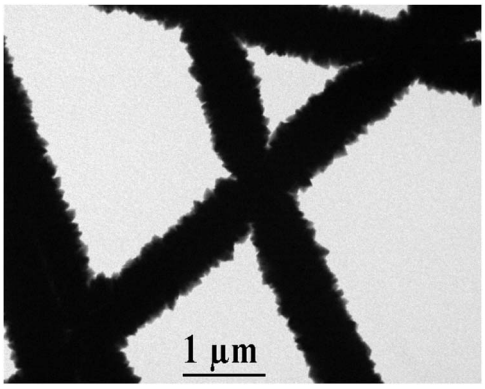

FIG. 6. Coating morphology near the locations where the fibers cross.

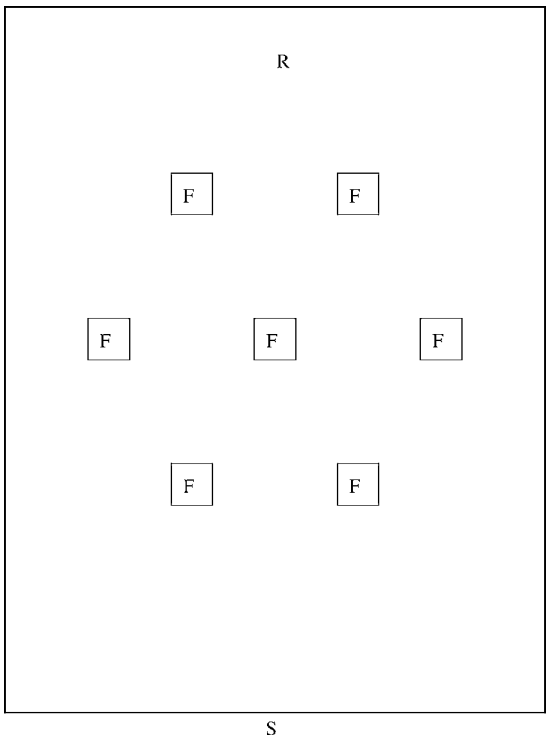

FIG. 7. Domain R with a source at S and seven fibers F perpendicular to the page.

vector at a boundary point (x,y) such that it is directed into the interfiber space. The governing equations are

$$c_t = \hat{D}(c_{xx} + c_{yy}), \quad (x,y) \in R, \tag{18}$$

$$\hat{D}c_{\mathbf{n}} = kc - \omega k_{\text{ions}}, \quad (x,y) \in S, \tag{19}$$

$$c_{\mathbf{n}} = 0, \quad (x,y) \in \partial R - S - \partial F, \tag{20}$$

$$\hat{D}c_{\mathbf{n}} = k_F c, \quad (x,y) \in \partial F, \tag{21}$$

$$c = 0, \quad (x,y) \in R \text{ at } t = 0. \tag{22}$$

As before, $\hat{D}$ is the diffusivity, k and k_F are the reaction coefficients for deposition onto the target and substrate, respectively, and k_{ions} is the desorption rate resulting from ion bombardment. For simplicity we take $k=k_F$. For $t \in [0,60]$, ω is increased linearly from 0 to 1; for $t > 60$ s we take $\omega = 1$. This is needed to achieve convergence of the numerical solution.

Through numerical simulation we investigate the variation of the concentration c resulting from the density of the fiber cluster. The initial-value problem is solved numerically using the FORTRAN subroutine VLUGR2 (Ref. 9) and the results are displayed using MATLAB. R is taken to be 1700 nm high and 1300 nm wide. The fibers F are 100 nm by 100 nm. The diffusivity $\hat{D}$ is taken to be 7.5×10^{13} nm^2/s. Unless stated otherwise, we take $k = 3 \times 10^{11}$ nm/s and $k_{\text{ions}} = 5 \times 10^{-26}$ mol/nm^2 s. In this case the value of c at the source S is $c = 1.67 \times 10^{-37}$ mol/nm^3. Simulations are run for 120 s.

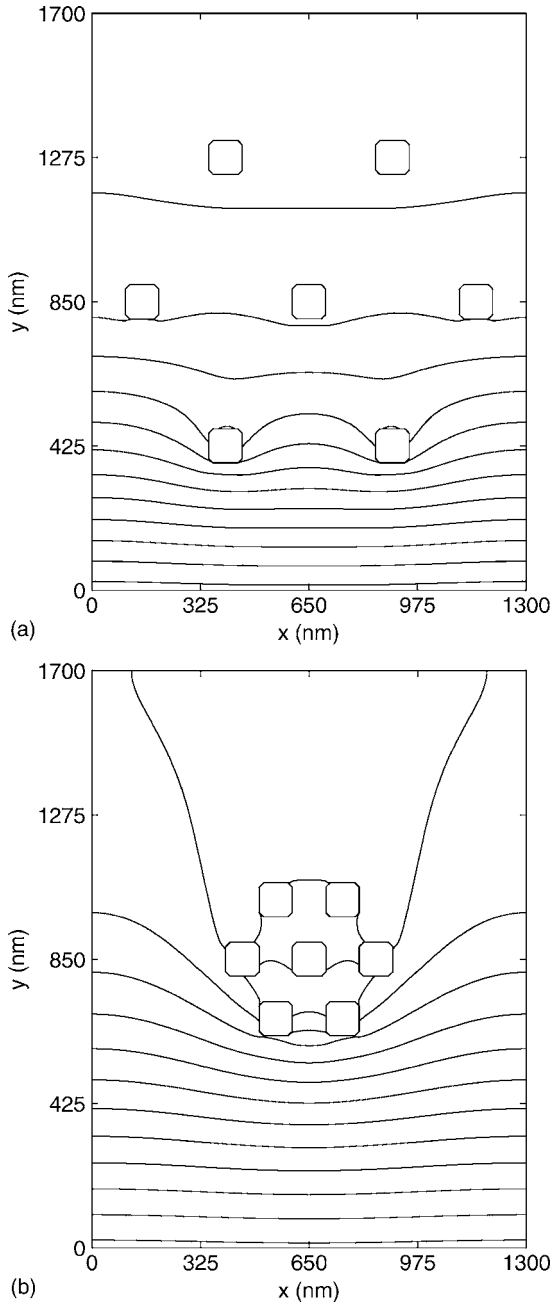

FIG. 8. Effect of fiber spacing on concentration as seen in contour plots. Spacing at (a) 500 and (b) 200 nm.

B. Results

Simulations are performed with fiber spacings of 500 and 200 nm, measured center to center. The results are shown in Figs. 8–10. The left-hand graphs have 500 nm fiber spacings and the right-hand graphs have 200 nm spacings. In Fig. 8 contour lines are spaced 1×10^{-38} mol/nm^3 apart. In Fig. 8(a) we note that there are local concentration changes in the vicinity of a fiber, but these effects do not extend to other fibers. However, Fig. 8(b), with smaller fiber spacings, shows that the effect of a fiber on the concentration can extend to nearby fibers. A simulation using fibers spaced 300 nm apart also shows that the effect on concentration extends to nearby fibers. For both plots in Fig. 8, note also the dif-

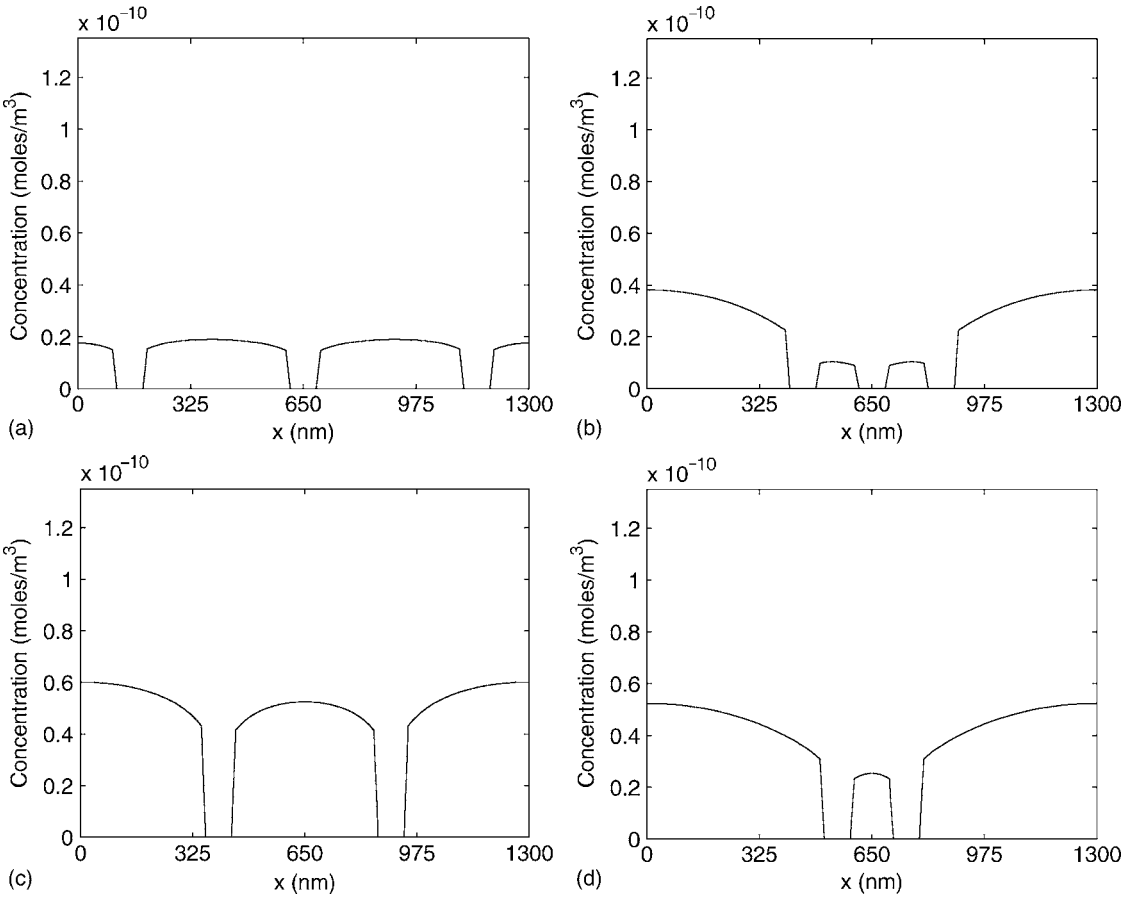

FIG. 9. Effect of fiber spacing on concentration as seen in horizontal traces through the middle and lower rows of fibers as shown in Fig. 8. (a) Middle row: spacing at 500 nm, (b) middle row: spacing at 200 nm; (c) lower row: spacing at 500 nm, and (d) lower row: spacing at 200 nm.

ference in concentration between the side of a fiber that faces the source S and the opposite side. This effect is most pronounced at the fibers, which are closest to S.

Figure 9 illustrates the magnitude of the fiber interaction in horizontal traces through a row of fibers. The fibers are located where the concentration is zero. The upper row of graphs shows traces through the middle row of fibers, whereas the lower row of graphs shows traces through the lower row of fibers. A difference in concentration is observed across the end fibers in the right-hand graphs, but little such difference is seen in the left-hand graphs. This effect is most pronounced in the upper-right-hand graph where the fibers are spaced 200 nm apart and the middle fiber is surrounded by fibers above and below as well as to the left and right.

In Fig. 10 the upper graphs show vertical traces through the middle fibers and the lower graphs show vertical traces through the two fibers to the left of center. Note that the fiber closer to the source shows a large relative change in concentration from one side to the other.

Next we examine the effect of increasing the rate of deposition. In Figs. 11(a), 12(a), and 13(a) we take, as before, $k=3\times10^{11}$ nm/s and $k_{\text{ions}}=5\times10^{-26}$ mol/nm^2 s; and in Figs. 11(b), 12(b), and 13(b) $k=7.5\times10^{13}$ nm/s. We adjust the value of k_{ions} so the ratio k_{ions}/k is the same for both values of k. Thus, we take $k_{\text{ions}}=1.25\times10^{-23}$ mol/nm^2 s in Figs. 11(b), 12(b), and 13(b). In Fig. 11 the contour lines are spaced 1×10^{-38} mol/nm^3 apart. Fig. 11(b) shows a larger concentration gradient between the source and the lower fibers. Note also the nearly constant concentration above the middle row of fibers.

Figure 12 shows that for the larger value of k the concentration has been reduced nearly to zero near the fibers in the second row. There is no visible difference in concentration observed across the end fibers in either graph of Fig. 12. Fig. 13(b) shows that the coating material has been nearly depleted from the region behind the center fiber.

C. Multiple fiber coating conclusions

From the numerical simulations of coating onto an array of fibers we see the following:

(1) In high porosity configurations where the fibers are approximately spaced five times their diameter (center to center) or more, the concentration field of depositing material around fibers the same distance from the source is more uniform than low porosity configurations. Further, due to deposition, the concentration field decreases in magnitude with distance from the source. Hence, it appears that in high porosity configurations the deposition onto a fiber is independent of the other fibers in the cluster. In this case a model for deposition onto a single fiber, with a uniform source (in the angular direction) of depositing material around the fiber, will be relevant.
(2) In low porosity configurations, the concentration field is

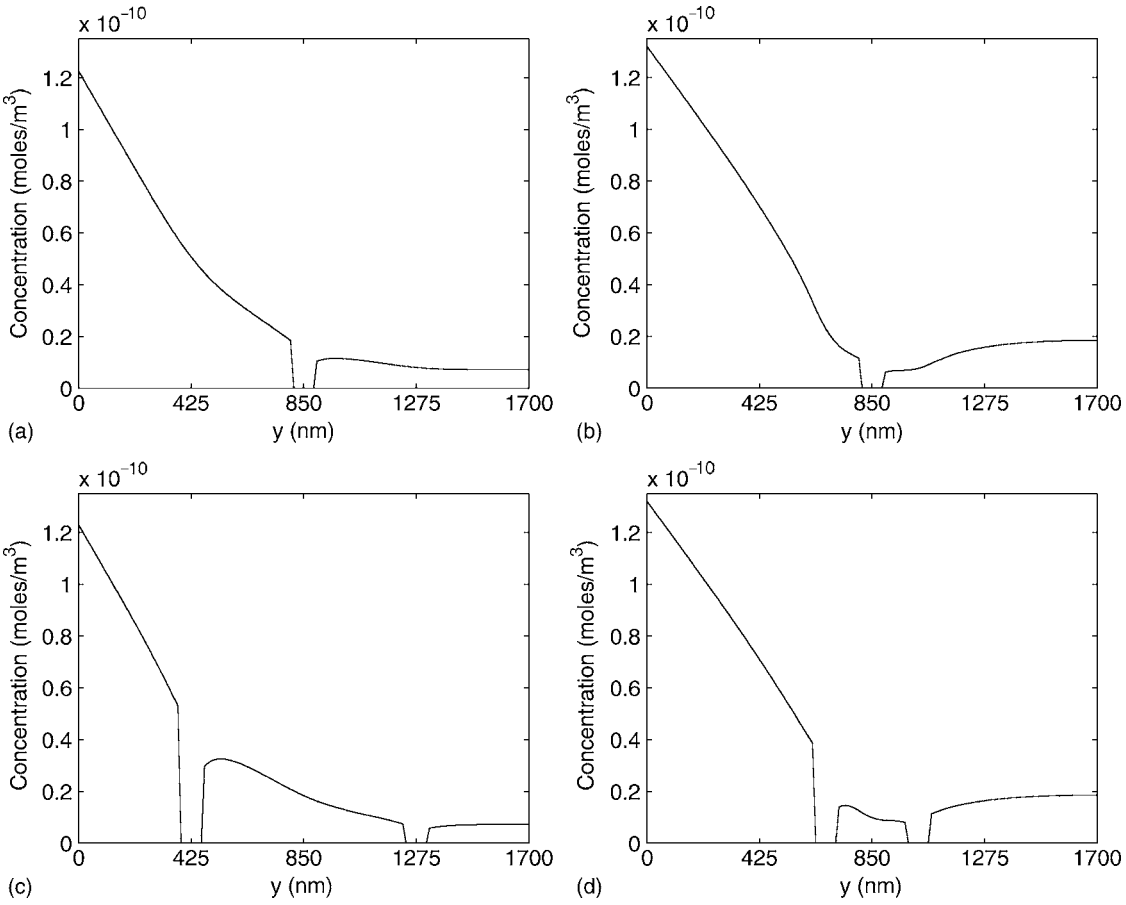

FIG. 10. Effect of fiber spacing on concentration as seen in vertical traces through the middle fiber and the two fibers to the left of center as shown in Fig. 8. (a) Middle fiber: spacing at 500 nm, (b) middle fiber: spacing at 200 nm, (c) fibers left of center: spacing at 500 nm, and (d) fibers left of center: spacing at 200 nm.

not uniform around a fiber. The concentration is higher at edges of the fiber that are nearer to the source. In this case a model that accounts for angular variation in the source of depositing material will be relevant. Figure 14 displays the morphology $F(\theta,t)$ of the coating predicted by numerical simulations using the standard parameter set (17) with C^* modified to $C^*[1-0.15\sin(\theta)]$. The latter modification allows for higher concentration near the bottom (nearer to the target) of the fiber. This 15% relative variation at the outer boundary yields an initial concentration at the coating surface that varies from 0.094 to 0.122 with a mean of 0.107—about a 13% relative variation. The average coating growth after 3 min is 5.23 nm, with an average of 4.93 nm near the top ($\theta=\pi/2$) and 5.54 nm near the bottom ($\theta=3\pi/2$)—almost a 6% relative variation.

(3) As the deposition rate, measured by k, increases, the concentration field decreases significantly with distance from the source.

(4) In low porosity configurations, lower concentration is found near fibers in the middle of the cluster than around fibers near the outside edge of the cluster as compared with high porosity configurations. This leads to larger concentration gradients around the fibers in the low porosity configuration that could result in more deposition on interior fibers of the cluster.

IV. COMPARISON OF NUMERICAL SIMULATION RESULTS WITH EXPERIMENTAL OBSERVATIONS

References 2 and 3 focused on the influence of model parameters on the coating thickness, morphology, and wavelength. Basic results indicate that when D_{k_F} is large, the deposition dominates and bumps will grow, leading to a rough surface. When D_{k_F} is small, diffusion dominates and dips will fill in faster, leading to a smoother surface. We continue evaluation of the model predictions by comparing experimental observations of the general trends of coating thickness and morphology (roughness) to parameter changes with model predictions.

A. Experimental observations

A Denton physical vapor deposition chamber was used to deposit films onto nanofiber substrates. The system was pumped using a turbomolecular pump and the base pressure of the system was 1×10^{-6} Torr. The materials were deposited using a 2 in. aluminum sputtering source mounted on a Mini-Mak radio frequency magnetron sputtering gun. rf power ranged between 30 and 150 W and was controlled using the Mini-Mak system. The total pressure in the system during the deposition ranged from 4 to 40 mTorr and was controlled by the flow rate of argon into the system and

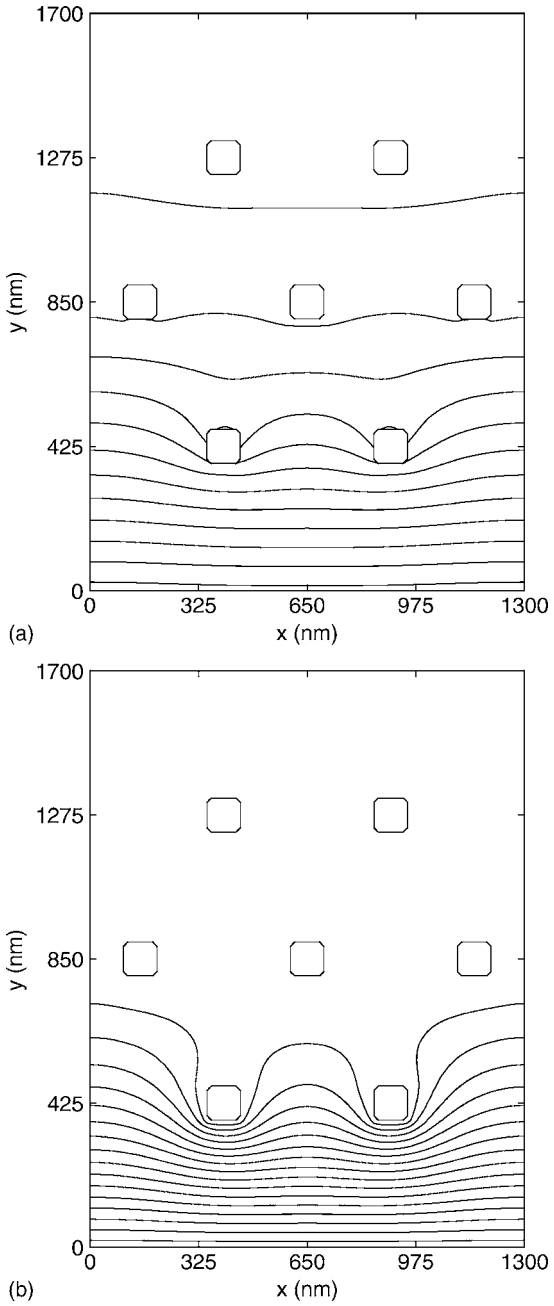

FIG. 11. Effect of k on concentration as seen in contour plots for fibers with 500 nm spacing. (a) $k=3\times10^{11}$ nm/s and (b) $k=7.5\times10^{13}$ nm/s.

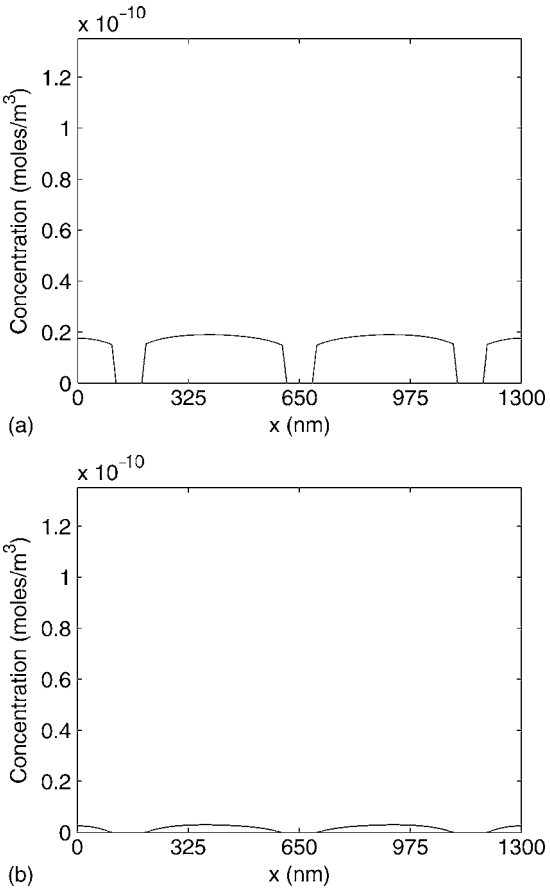

FIG. 12. Effect of k on concentration as seen in horizontal traces through the middle row of fibers as shown in Fig. 11. (a) $k=3\times10^{11}$ and (b) $k=7.5\times10^{13}$ nm/s.

measured using a baratron gauge from MKS. Nylon-6 nanofibers were electrospun onto copper TEM grids to facilitate the imaging of the coated surface. The nanofibers were then placed in the deposition chamber on a stainless steel plate. The stainless steel plate was held above the sputtering target at a distance of 8 cm with no applied bias voltage. The temperature of the stainless steel plate was not controlled. A Sycon STM-100/MF thickness/monitor with quartz crystal microbalance was used to estimate the deposited film thickness during deposition.

Deposition rate was determined using TEM images of the coated fiber. The thickness of the coating was determined based on the location of the interface between the fiber and the coating. The fiber can be seen in the interior of the TEM images in Fig. 2. Several thicknesses were determined along the length of the fiber to get an average deposition rate. These deposition rates were then compared to rates measured by a quartz crystal microbalance mounted just near the fibers during deposition. The rates were comparable. In some cases the coated nanofibers were heated after the coating had been applied to remove the nylon nanofiber. These samples indicated that the coating was continuous around the nanofiber and that the coating thickness did not vary significantly along the circumference.

The porosity of the fiber mesh was determined based on a ratio of the area in the TEM image occupied by the fiber and the total area of the image. We assume that the nanofiber mesh being coated was a single, nonwoven layer on the TEM grid. The porosity values are used to determine the average fiber spacing, defined as $\hat{S}_F$ in the model. There is a critical $\hat{S}_F$, or interaction distance that can be seen in Fig. 6. At locations where the fibers are closer than the critical $\hat{S}_F$ and the coating has become thick enough for noticeable changes in the coating thickness, one can see a pinching off of the coating. This pinching off indicates that the adjacent fibers within the critical $\hat{S}_F$ are influencing the concentration field around the fibers. The simulations conducted in Sec. III that predict a critical $\hat{S}_F$ of around 2.5 times the fiber diameter are consistent with these observations.

Images of the coated nanofiber from the TEM analysis were used to determine the roughness of the coated nanofi-

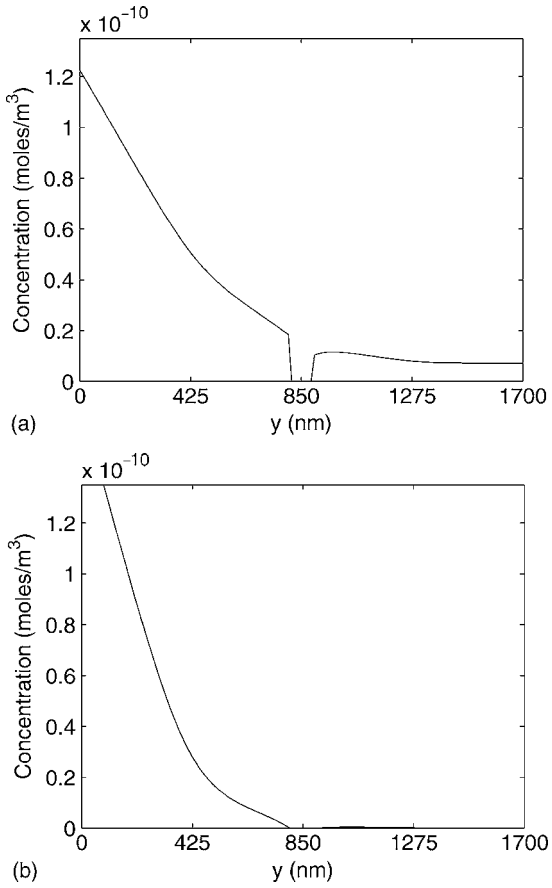

FIG. 13. Effect of k on concentration as seen in vertical traces through the middle fiber as shown in Fig. 11. (a) $k=3\times10^{11}$ and (b) $k=7.5\times10^{13}$ m/s.

bers. To determine the roughness, the thickness of the coating was determined at several points along the length of the nanofiber. The root mean square (rms) roughness of the coating was determined using the following equation:

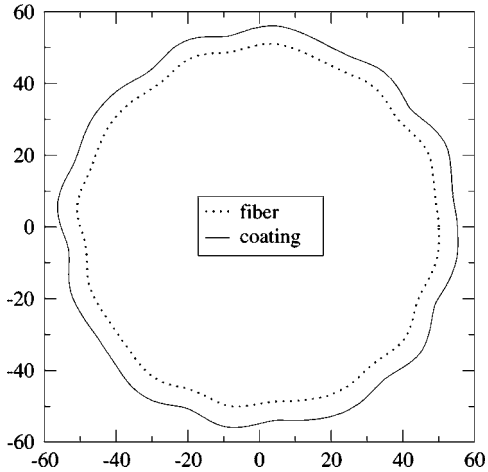

FIG. 14. Coating morphology $F(\theta,t)$ of the coating predicted by numerical simulations using the standard parameter set (17) with C^* modified to $C^*[1-0.15\sin(\theta)]$.

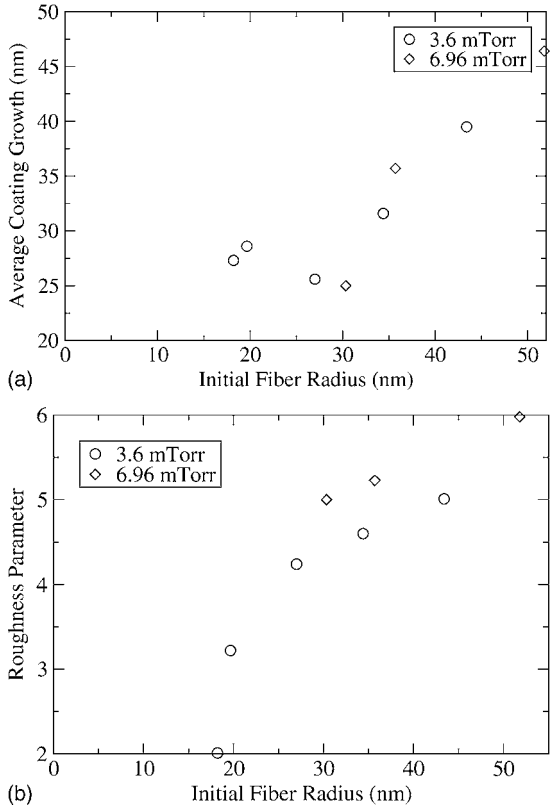

FIG. 15. Experimental observation of the effect of pressure on the thickness and roughness of the coating after 6 min of growth (power=90 W, 55% porosity). (a) Coating thickness and (b) coating roughness.

$$rms = \sqrt{\frac{1}{n}\sum_{j=1}^{n}(h(z_j)-\bar{h})^2}, \tag{23}$$

where n is the number of points used, $h(z_j)$ is the height at point z_j along the length, and $\bar{h}$ is the average thickness of the coating on the nanofiber:

$$\bar{h} = \frac{1}{n}\sum_{j=1}^{n} h(z_j). \tag{24}$$

The rms roughness calculations were made with respect to length. The modeling we have done to describe this process, however, will determine a roughness with respect to angle around the circumference of the fiber. To determine the uniformity of this roughness around the circumference, roughness values were determined at different beam angles (from −15° to 15°) with respect to the plane of the fiber in the TEM chamber. Roughness calculations along the length of the fiber were made at several beam angles and then compared. There was almost no variation in the roughness along the length of the fiber as the beam angle was changed. This analysis suggests that our roughness estimates are valid for at least 30° slices of the coating surface.

Figures 15–17 display the influence of pressure, power, and mat porosity on the coating thickness and roughness as a function of the fiber diameter. General trends indicate that the coating thickness increases with increasing fiber diameter, although in Figs. 15 and 16 the data suggest an initial decrease in thickness for smaller diameter fibers. The coating

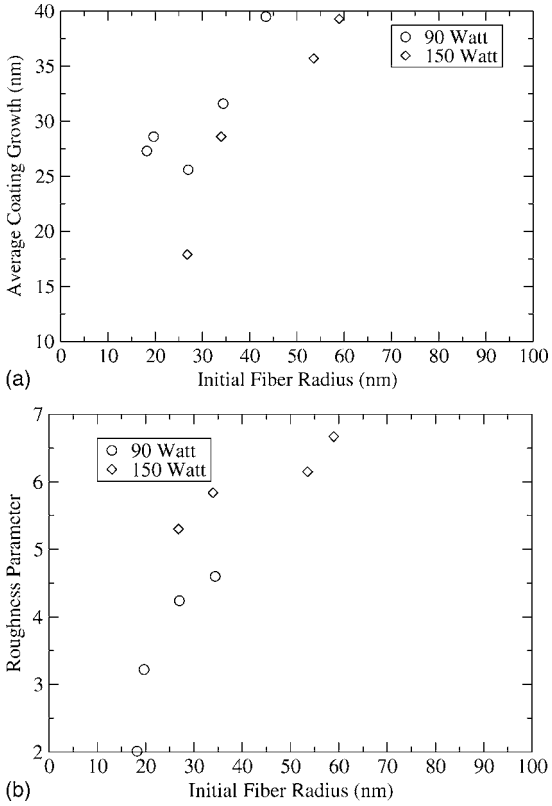

FIG. 16. Experimental observation of the effect of power on the thickness and roughness of the coating after 6 min of growth (pressure=3.6 mTorr, 55% porosity). (a) Coating thickness and (b) coating roughness.

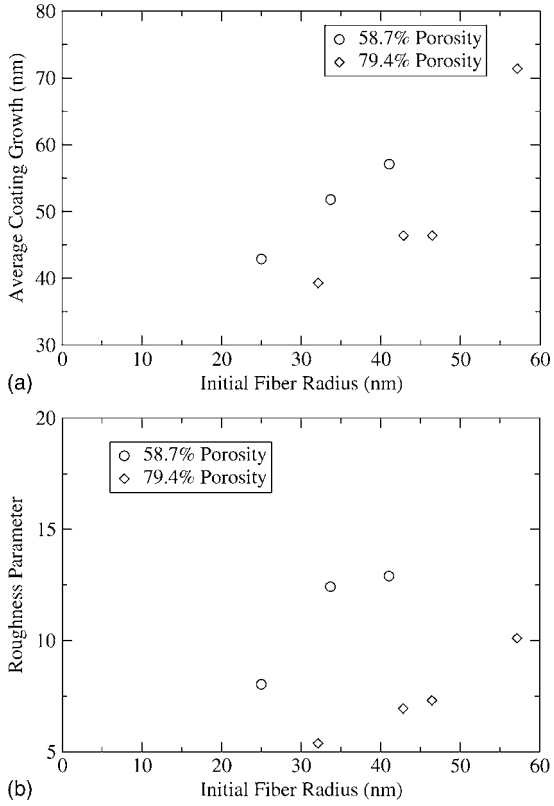

FIG. 17. Experimental observation of the effect of mat porosity on the thickness and roughness of the coating after 6 min of growth (power =90 W, pressure=3.6 mTorr). (a) Coating thickness and (b) coating roughness.

thickness also increases with increasing pressure, and increases with decreasing mat porosity and decreasing power. The latter observation is counterintuitive and may be due to an increase in etching of the coating surface at higher power per the discussion for Fig. 23. General trends indicate that the roughness increases with increasing fiber diameter, increases with increasing pressure and power, and increases with decreasing mat porosity. The roughness seems to be most sensitive to porosity and then fiber radius; a 20% change in porosity leads to a twofold increase in roughness and a twofold increase in radius leads to almost a twofold increase in roughness.

B. Numerical simulation results

We define a roughness parameter ρ at time t to measure variations in the coating morphology from a circular coating shape:

$$\rho = \sqrt{\frac{1}{M}\sum_{j=1}^{M}\left(F(\theta_j,t) - \bar{F}(t)\right)^2}. \tag{25}$$

Here the average radius $\bar{F}$ of the circular coating shape is

$$\bar{F}(t) = \frac{1}{M}\sum_{j=1}^{M} F(\theta_j,t). \tag{26}$$

Using the value of the average radius $\bar{F}$ after 3 min of coating and the original fiber radius, we determine the thickness of the coating. Three minutes of simulated coating is sufficient to see the trends and is completed in reasonable CPU time.

Equation (17) lists the standard parameter set for numerical solutions of the model. This parameter set is varied as follows in order to simulate changes in operating parameters:

(1) High power—C^* is changed from 1.5×10^{-36} to 4.5×10^{-36} mol/nm^3. $k_{F_{\text{ions}}}$ is changed from 5.58×10^{-26} to 26×10^{-26} mol/nm^2 s.
(2) High pressure—C^* is changed from 1.5×10^{-36} to 1.6×10^{-36} mol/nm^3. $\hat{D}$ is changed from 4×10^{13} to 3×10^{13} nm^2/s.
(3) High porosity—$\hat{S}_F$ is changed from 300 to 400 nm.

These changes have been calculated using the data in Fig. 4 together with the figures in Refs. 1 and 2 as discussed in Sec. II. Also as discussed in Sec. II, the initial polymer nanofiber landscape is taken to be a superposition of Fourier modes. We find that changing the amplitude of these modes (which defines the initial roughness of the polymer nanofiber) slightly influences the coating thickness. However, changing the amplitude of the modes significantly alters the coating roughness. If one doubles the amplitude of the modes, effectively doubling the initial roughness of the nanofiber, then the resulting coating roughness is nearly doubled.

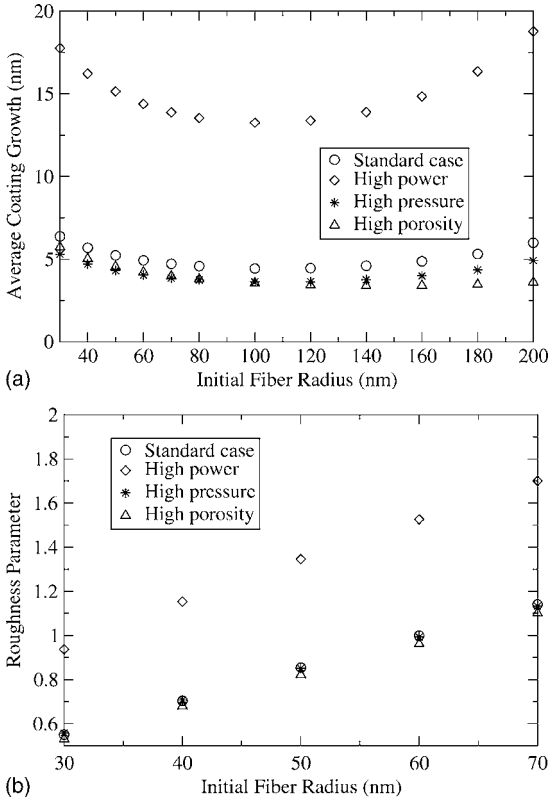

FIG. 18. Effect of power, pressure, and porosity on the thickness and roughness of the coating. (a) Coating thickness and (b) coating roughness.

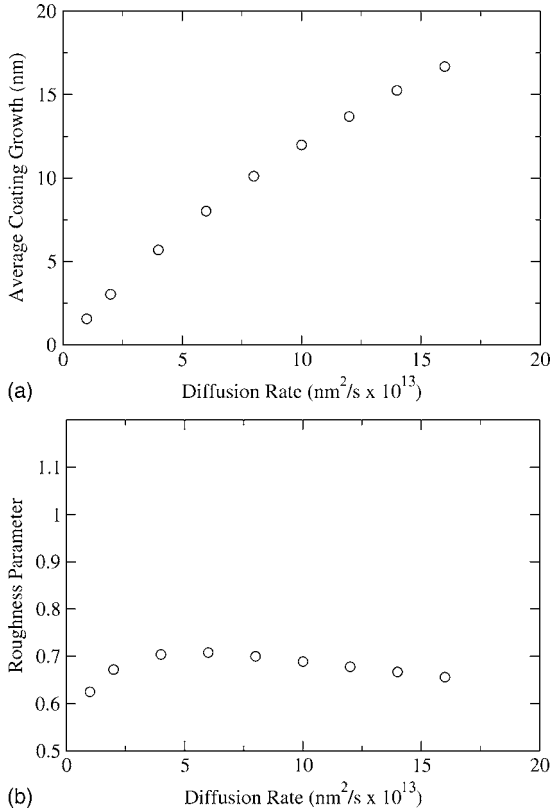

FIG. 19. Effect of $\hat{D}$ on the thickness and roughness of the coating. (a) Coating thickness and (b) coating roughness.

Figure 18 displays the influence of pressure, power and mat porosity on the coating thickness and roughness as a function of the fiber diameter. Simulation results are generally consistent with the experimental observations in Figs. 15–17. General trends indicate that the coating thickness decreases with increasing initial fiber diameter for smaller diameters. The thickness, though, eventually increases with increasing diameter for a fixed value of $\hat{S}_F$. The explanation for this behavior is that the smaller diameter surface area allows for a thicker coating on smaller fibers. However, the coating surfaces of larger fibers are nearer to the concentration source at $\hat{S}_F$ and thus experience an increase in deposition. General trends indicate that the roughness increases with increasing fiber diameter, increases with increasing pressure and power, and increases with decreasing mat porosity. The roughness is most sensitive to variations in the fiber diameter and power. The increase in roughness with increasing fiber diameter is due to the availability of higher levels of concentration as the coating surface is nearer to the source location where the concentration has the fixed value C^*. The increase in roughness with power is due to the higher value of C^* as discussed in Sec. II. The slight change in roughness with pressure is due to the slight changes of the ion density with pressure as shown in Fig. 4. The slight decrease in roughness with increases in mat porosity is not as distinct as the experimental observations in Fig. 17.

Figure 19 displays the influence of mass diffusivity on the coating thickness and roughness as a function of the fiber diameter. General trends indicate that the coating thickness increases with increasing diffusivity due to the increased

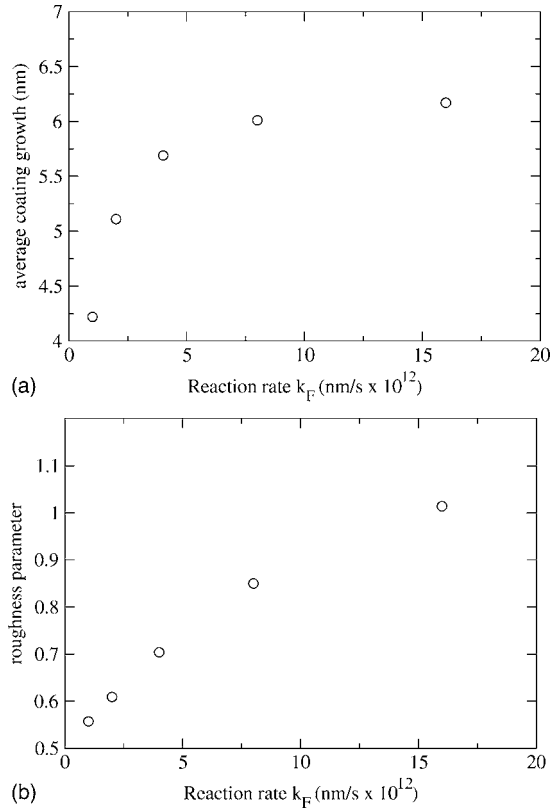

FIG. 20. Effect of k_F on the thickness and roughness of the coating. (a) Coating thickness and (b) coating roughness.

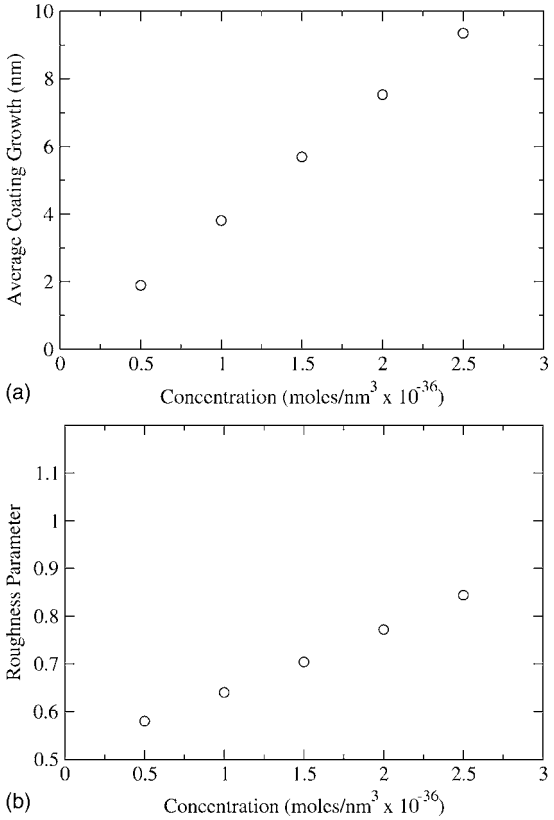

FIG. 21. Effect of C^* on the thickness and roughness of the coating. (a) Coating thickness and (b) coating roughness.

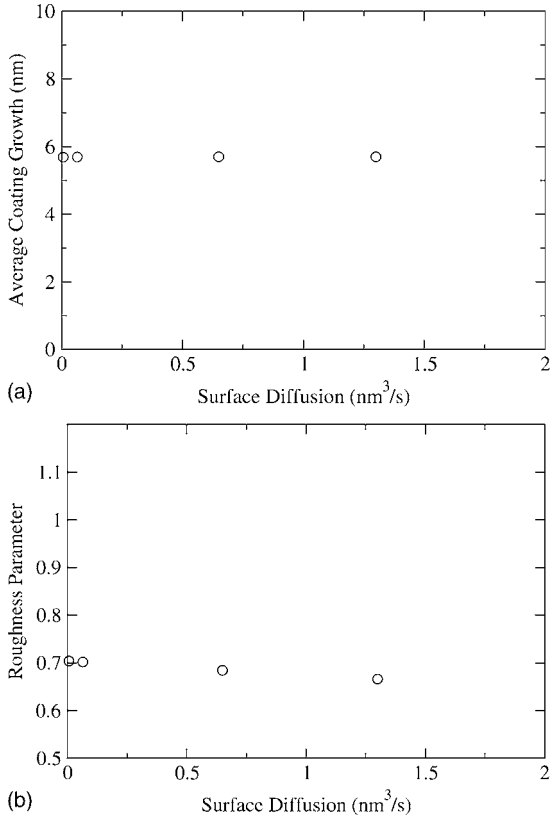

FIG. 22. Effect of $\psi_s D_s$ on the thickness and roughness of the coating. (a) Coating thickness and (b) coating roughness.

transport of coating material to the surface. General trends indicate that the roughness slightly decreases with increasing diffusivity due to the more uniform concentration of coating material with increased diffusive transport.

Figure 20 displays the influence of the deposition or sticking parameter on the coating thickness and roughness as a function of the fiber diameter. General trends indicate that the coating thickness increases with an increase in the attachment rate. General trends indicate that the roughness also increases with the attachment rate.

Figure 21 displays the influence of concentration on the coating thickness and roughness as a function of the fiber diameter. General trends indicate that the coating thickness and roughness increase substantially with increasing values of C^*.

Figure 22 displays the influence of surface diffusion on the coating thickness and roughness as a function of the fiber diameter. General trends indicate that the coating thickness is not affected by changes in the surface diffusion of coating material. General trends indicate that the roughness decreases slightly with increasing surface diffusion. This stabilizing trend was discussed in Ref. 3.

Figure 23 displays the influence of the sputtering or etching parameter on the coating thickness and roughness as a function of the fiber diameter. General trends indicate that the coating thickness and roughness decrease with increases in this etching effect.

V. SUMMARY AND CONCLUSION

The coating of nanoscale structures and the evolution of crystalline structure at the nanoscale are and will continue to

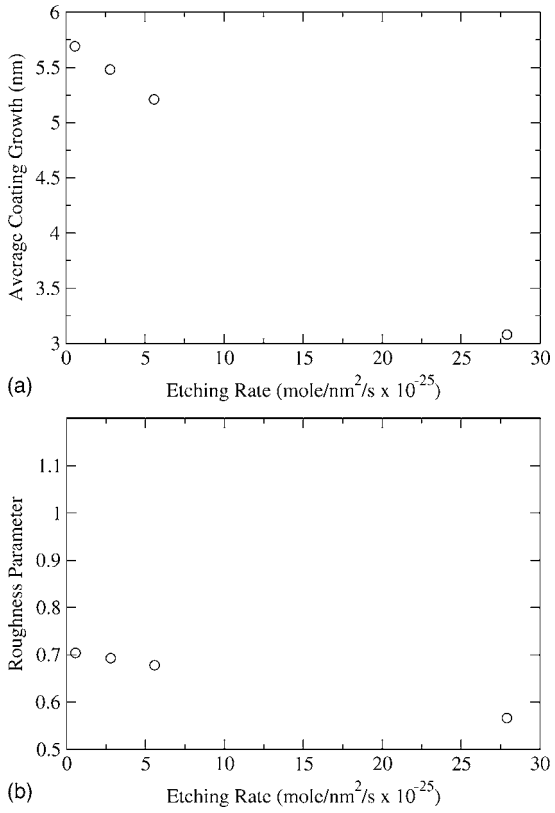

FIG. 23. Effect of $k_{F_{\text{ions}}}$ on the thickness and roughness of the coating. (a) Coating thickness and (b) coating roughness.

be important issues. We develop a comprehensive model integrating across atomic to continuum length scales for simulating the sputtering, transport and deposition of coating material onto a nanoscale substrate.[1–3] In this article the influence of power, pressure and mat porosity processing factors is examined. From the mat porosity simulations, it appears that the single fiber model is valid when the center to center distance between fibers is greater than about five times the diameter of the fibers. Otherwise, a multiple fiber model is needed to capture the interaction of neighboring fibers on the concentration field.

Based upon the benchmarking studies of the model against experimental data as processing parameters are varied, it appears that the model we have developed predicts trends for the coating evolution on nanoscale structures that agree with experimental observation. Operating conditions that lead to high values of coating concentration C^* result in thicker and rougher coatings. The coating thickness also increases with increasing initial fiber diameter. The coating roughness increases with increasing initial fiber diameter, pressure and power, and decreasing mat porosity. However, increases in power lead to an increase in etching at the coating surface. This could result in a decrease in coating thickness.

Based upon the parametric study of material parameters it appears that systems characterized by high diffusive transport of material, high surface diffusion and high etching of coating material will have smoother coatings. On the other hand, systems characterized by high attachment rates will have rougher coatings.

The computational simulations presented here are limited to single-valued coating morphologies. Hence, we do not simulate the nodular structures shown in Fig. 2. As the coating first develops a mushroom type shape, the pinching together of the peaks may result in a further reduction of concentration in the valleys. This would cause the peaks to grow faster than the valleys and a finger-like formation may occur as a result. This phenomenon, known as self-shadowing, has also been considered by Ref. 10 through the inclusion of relevant view factors for the impinging concentration flux over the surface, and by Refs. 11–13 for coating onto flat surfaces. Additionally, one needs to further investigate the influence of the morphology of the coating surfaces on the molecular dynamics simulations used to obtain the reaction and desorption coefficients, k_F and $k_{F_{\text{ions}}}$.

With a validated model we can begin to predict how coating properties will change with deposition conditions for similar geometries. This predictive capability will be quite useful as the size of solid state optoelectronic components continues to decrease.

ACKNOWLEDGMENTS

This work was supported by NSF Grant No. DMI-0403835 and NASA Grant No. NNC-04GB27G.

[1] A. Buldum, I. Busuladzic, C. B. Clemons, L. H. Dill, K. L. Kreider, G. W. Young, E. A. Evans, G. Zhang, S. I. Hariharan, and W. Keifer, J. Appl. Phys. **98**, 044303 (2005).
[2] A. Buldum, C. B. Clemons, L. H. Dill, J. Heminger, K. L. Kreider, G. W. Young, X. Zheng, E. A. Evans, G. Zhang, and S. I. Hariharan, J. Appl. Phys. **98**, 044304 (2005).
[3] K. Moore, C. Clemons, K. Kreider, and G. Young, J. Appl. Phys. **101**, 064305 (2007).
[4] W. Liu, M. Graham, E. A. Evans, and D. H. Reneker, J. Mater. Res. **17**, 3206 (2002).
[5] A. L. Yarin, S. Koombhongse, and D. H. Reneker, J. Appl. Phys. **90**, 4836 (2001).
[6] A. L. Yarin, S. Koombhongse, and D. H. Reneker, J. Appl. Phys. **89**, 3018 (2001).
[7] M. A. Lieberman and A. J. Lichtenberg, *Principles of Plasma Discharges and Materials Processing* (Wiley, New York, 1994).
[8] P. Hamrick, Master's thesis, The University of Akron, Akron, OH, 2006.
[9] J. Blom, R. Trompert, and J. Verwer, ACM Trans. Math. Softw. **22**, 302 (1996).
[10] O. A. Louchev, Y. Sato, and H. Kanda, J. Appl. Phys. **89**, 2151 (2001).
[11] J. Thiart and V. Hlavacek, J. Comput. Phys. **125**, 262 (1996).
[12] J. Thiart and V. Hlavacek, AIChE J. **41**, 1926 (1995).
[13] G. S. Bales, A. C. Redfield, and A. Zangwill, Phys. Rev. Lett. **62**, 776 (1989).